Insights into the role of wettability in cathode catalyst layer of proton exchange membrane fuel cell; pore scale immiscible flow and transport processes

H. Fathi [a], A. Raoof [b, *], S.H. Mansouri [a]

[a] Department of Mechanical Engineering, Shahid Bahonar University of Kerman, 7616914111, Kerman, Iran
[b] Department of Earth Sciences, Utrecht University, P.O. Box 80021, 3508 TA, Utrecht, The Netherlands

HIGHLIGHTS

- Two-phase flow processes in cathode catalyst layer are modelled at the pore scale.
- The effects of hydrophilic and hydrophobic conditions are explored.
- Diffusivity, available surface area, and oxygen consumption rate are calculated.
- Final saturation of 0.28 was obtained for contact angle of 150 due to water removal.

ARTICLE INFO

ABSTRACT

The production of liquid water in cathode catalyst layer, CCL, is a significant barrier to increase the efficiency of proton exchange membrane fuel cell. Here we present, for the first time, a direct three-dimensional pore-scale modelling to look at the complex immiscible two-phase flow in CCL. After production of the liquid water at the surface of CCL agglomerates due to the electrochemical reactions, water spatial distribution affects transport of oxygen through the CCL as well as the rate of reaction at the agglomerate surfaces. To explore the wettability effects, we apply hydrophilic and hydrophobic properties using different surface contact angles. Effective diffusivity is calculated under several water saturation levels. Results indicate larger diffusive transport values for hydrophilic domain compared to the hydrophobic media where the liquid water preferentially floods the larger pores. However, hydrophobic domain showed more available surface area and higher oxygen consumption rate at the reaction sites under various saturation levels, which is explained by the effect of wettability on pore-scale distribution of water. Hydrophobic domain, with a contact angle of 150, reveals efficient water removal where only 28% of the pore space stays saturated. This condition contributes to the enhanced available reaction surface area and oxygen diffusivity.

1. Introduction

Proton exchange membrane fuel cells, PEMFCs, show a great potential as a cleaner replacement for several different portable power suppliers such as internal combustion engines and Lithium-ion batteries [1]. PEMFCs have several advantages including high-energy density at low operating temperatures and quick start-up, while they have zero emissions. However, to be competitive with the traditional energy convertors, PEMFCs should be improved to offer higher performance and lower losses. It is a clearly established fact that the major losses in PEMFCs are happening within the cathode catalyst layer, CCL, where the liquid water is produced [2]. The liquid water, as the product of the electrochemical reactions, floods the pore spaces of CCL to block the reaction sites at the three-phase regions composed of carbon covered by platinum particles, oxygen, and ionomer. Possibility of two undesirable extreme conditions in CCL, i.e., dehydration of membrane and flooding of pores, highlights the necessity of finding an optimum water management within the fuel cell [3].

Much research work has been devoted to enhance the performance of PEMFC through simplifying the complex processes such

* Corresponding author.
E-mail address: a.raoof@uu.nl (A. Raoof).

as neglecting the presence of water as an immiscible liquid phase in CCL [4–12], the consequence of which was not evaluated. Some of these studies assumed that a well-humidified ionomer is the only barrier against oxygen diffusion in CCL [4–7], while some other assumed water in the form of vapor phase and having no effect on oxygen diffusion [8–12]. The results obtained by applying these assumptions often overpredicted the diffusivity values [13] as water flooding in CCL is the main barrier towards oxygen consumption, in particular at high saturation levels. Therefore, it is needed to include the effect of the produced water in CCL as an immiscible liquid phase within numerical simulations [14].

Several methods have been applied to include the presence of liquid water in CCL, which may be categorized into two major groups. The first group assumed a priori homogenous distribution of water [2,15–22] and considered oxygen dissolution into this phase by applying Henry's law [23] or oxygen diffusion through the partially saturated domain using Bruggeman correlation [24]. For example, Bernardi and Verbrugge [15] investigated the production of the liquid water in CCL by applying a 1D homogenous continuum-scale model and calculated the dissolution of oxygen in ionomer and the liquid water. Springer et al. [2] found agreement between their model and experimental results for well-humidified PEMFC by considering thin-film catalyst layers bonded directly to the membrane. They approximated the effect of liquid water on the transport of oxygen by changing the effective porosity of the gas diffusion layer (GDL). Marr and Li [16] considered the ionomer layer surrounding the catalyst particles to be fully hydrated, and the void region in the catalyst layer to be completely flooded by the liquid water. They assumed the dissolved oxygen first diffuses through the liquid water and then through the thin ionomer before reaching the reaction sites. Following the study of Mar and Li [16], Baschuk and Li [17] applied the same formulation and calculated the flux of oxygen for different degrees of water flooding in CCL and its effect on the diffusivity of oxygen by applying the Bruggeman correlation. To obtain a more realistic distribution of water produced around the agglomerates, Hu et al. [25] considered presence of thin liquid water and ionomer films. Applying this assumption, they have performed a parametric analysis of PEMFC based on an agglomerate model for both anode and cathode catalyst layers.

In studies involved in the first group, no spatial distribution of the water phase based on two-phase transport were considered. For this reason, many other studies have applied two-phase flow continuum-scale models to investigate the liquid water transport in PEMFC [26–35]. In order to obtain the threshold current density needed to form liquid water at different temperatures, You and Liu [27] applied the two-phase flow simulations. They have used a 2D homogeneous domain of the PEMFC's cathode to obtain the distribution of water mass fraction in the two-phase mixture. Wang et al. [28] classified single- and two-phase regimes of water distribution and transport by a threshold current density corresponding to the first appearance of the liquid water at the membrane/cathode interface. They assumed when the cell operates above the threshold current density, the liquid water is appeared and a two-phase zone is formed within the porous cathode. Nam and Kaviani [29] studied the formation−distribution of the condensed water in diffusion medium of PEMFCs, and its tendency to reduce the local effective diffusivity to influence cell performance. They assumed a threshold saturation equal to 0.10 for the phase continuity in porous media. Lin et al. [31] developed a two-phase, one-dimensional model to investigate the effect of water flooding in the gas diffusion and catalyst layers of the cathode on the overall performance of fuel cell. They found that the lack of efficient water removal and the subsequent liquid water accumulation in the gas diffusion and

catalyst layers led to the electrode flooding of the media. They confirmed that the flooding situation in the catalyst layer was more severe than that in the gas diffusion layer since water generation is originated in the catalyst layer. Das et al. [33] developed a one-dimensional analytical solution of water transport across the CCL. They concluded that the liquid water production from the phase change process is negligible compared to the water production from the electrochemical process. In spite of mentioned studies on two-phase transport, the effect of CCL pore sizes and the configuration of the agglomerates in this layer on water distribution cannot be determined by continuum scale models.

Using statistical theory of random composite media, Eikerling [36] investigated the effects of composition, porous structure, wetting properties, and partial saturation on effective properties. It was shown that a CCL with a higher fraction of larger pores or a wider pore size distribution has a higher oxygen effective diffusivity. The reason could be the effect of larger pores which decreases the influence of Knudsen diffusion in the whole domain. Applying an experimentally obtained capillary pressure-saturation relationship, Mulone and Karan [37] approximated the pore size distribution of CCL taking into account the transition between hydrophilic and hydrophobic characteristics. They showed that the effective diffusivity of oxygen in a CCL with mixed wettability reduces by the increase of saturation. However, the rate of such a reduction was higher for the hydrophobic diffusivity compared to the hydrophilic one, as the larger pores are more favorable for the fluid to occupy.

Pore network modelling, PNM, provides opportunity to directly include the pore scale processes to explore two-phase flow at the pore scale and to drive macroscopic transport parameters [14,38,39]. Raoof and Hassanizadeh have shown that water saturation has a strong and non-linear effect on solute spreading in granular media [40]. El Hannach et al. [14] developed a PNM approach to study two-phase transport phenomena inside a porous structure representative of hydrophilic and hydrophobic CCLs. The electrochemical reactions were not included. They found that the total liquid saturation at the end of water invasion is lower for hydrophobic pore network. Since pore network model uses local rules, in particular for trapping and snap off processes, and applies simple geometries for complex and angular pore structures, more accurate representations of the pore spaces are needed to investigate fluid transports in CCL.

To the best of the authors' knowledge, there is a lack of pore scale two-phase flow simulation to investigate the effect of saturation evolution on the diffusivity as well as its effect on changing the available reaction surface area and oxygen consumption rate in hydrophilic and hydrophobic CCLs. Hutzenlaub et al. [41] investigated the effect of liquid water existence on oxygen diffusion and on specific reaction surface area in a hydrophilic and hydrophobic reconstructed CCL. However, to include the presence of water, they made a simplifying assumption that water is present within pores from the smallest to the largest pore sizes for the hydrophilic domain and vice versa for the hydrophobic one to prevent solving the two-phase flow problem. The electrochemical reactions and two-phase flow were not considered in their study and they assumed CCL to be either extremely hydrophilic or hydrophobic which may not be the condition for a real CCL [42].

The distribution of liquid water in a hydrophilic or a hydrophobic porous media is controlled by the contact angle at the solid surfaces which affects spreading of the liquid phases and the pore filling processes through capillary forces. Fig. 1a shows two different local distribution of water on the surface of agglomerate due to different contact angles. Pore scale distribution of water on
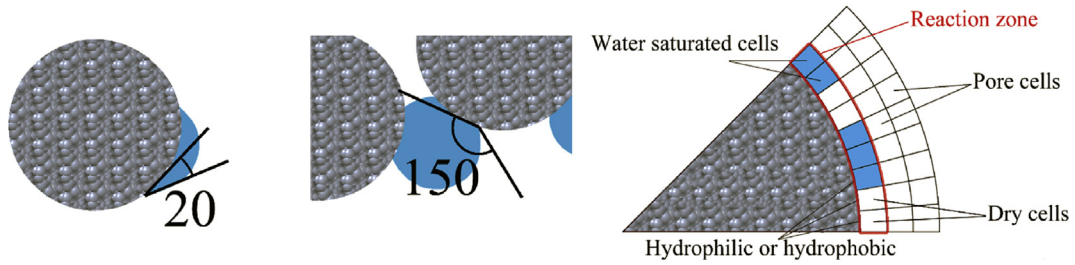
Fig. 1. a) schematic of different contact angles and water formation at the surface of agglomerates. The blue colour shows the liquid water. b) A schema of the numerical cells applied in the computational procedure. (For interpretation of the references to colour in this figure legend, the reader is referred to the web version of this article.)

the agglomerates controls the subsequent flow and the displacement of water which affects effective diffusivity as well as the available reaction surface areas for electrochemical reactions. Several experimental studies have investigated the effect of CCL with different distributions of polytetrafluoroethylene (PTFE) particles on the performance of the fuel cell [34,42–44]. The presence of PTFE in CCL increases the hydrophobicity of the layer. Nam and Kaviani [29] reported the intrinsic contact angle of PTFE to be about 108 and the apparent contact angle of CCL would be 120–140. The in-situ observations of dynamic meniscus front interface in Unitized regenerative fuel cell [45] and in alkaline fuel cell [46] have shown that the contact angle strongly depends on the solution pH level which can reduce the surface tension. The increase of overpotential can increase the pH value which causes the decrease of contact angle. However, it is shown that the assumption of static contact angle is reasonable when the overpotential is less than 0.4 [45,46], which is the choice of present study. Moreover, Yu et al. [42] showed that the contact angle in CCL has no significant variation by time.

In this study, we performed direct pore scale modelling to investigate transport of oxygen and the liquid water in CCL. The liquid water is produced at the surface of agglomerates, where the thin ionomer layer is assumed to have negligible effect on oxygen diffusion [9]. It was further assumed that reactions happen dominantly at the larger pores (the so-called secondary pores), which has been confirmed by several studies [14,35,41,47,48]. Production of water at the reaction surfaces in our model is controlled by the electrochemical reaction rate. Transport of oxygen through the CCL and its arrival and availability at the location of surface reaction sites determines the ultimate rate of electrochemical reaction. Increasing amount of water may hinder transport of oxygen through the domain, and, therefore, the reaction rate at the surfaces of agglomerates can decrease. This study shows, for the first time, the immiscible distribution of produced liquid water within CCL applying pore-scale two-phase flow formulations under different contact angles. By simulating under a wide range of water saturation, we calculated the evolution of several parameters including effective diffusivity, the available surface area which is not covered by the liquid water, as well as the oxygen consumption rate as functions of water saturation. Eventually, the water removal process was investigated for a hydrophobic domain to obtain the final water saturation of the CCL when the fuel cell operates under the steady-state condition.

2. Methodology

2.1. Governing equations

Transport of oxygen within the pore spaces of CCL which can be occupied by two phases (i.e., water and air phases), may be written as:

$$
\frac{\partial \left(s c_{O_2}^{w} + (1-s) c_{O_2}^{a} \right)}{\partial t} = \nabla \cdot \left(s D_{O_2}^{w} \left(\nabla c_{O_2}^{w} \right) \right) \\
+ \nabla \cdot \left((1-s) D_{O_2}^{a} \left(\nabla c_{O_2}^{a} \right) \right) + J_{O_2}
\tag{1}
$$

where $c_{O_2}^{w}$ and $c_{O_2}^{a}$ are oxygen concentrations in water and air, respectively, t is time, s is local volume fraction of water, $D_{O_2}^{w}$ and $D_{O_2}^{a}$ are the diffusion coefficients of oxygen in water and air, respectively, and J_{O_2} provides a sink term due to oxygen consumption in the electrochemical reactions. The concentration field is continuous and Henry's law may be applied to couple oxygen concentration at the air-water interfaces as [49,50]:

$$
c_{O_2}^{a} = H_{O_2}^{cc} c_{O_2}^{w}
\tag{2}
$$

where $H_{O_2}^{cc}$ is Henry's solubility constant. As pore length scales in CCL are typically nanoscale, the oxygen diffusivity is calculated by taking into account the contribution of binary diffusivity of oxygen-nitrogen, $D_{O_2-N_2}$, as well as the Knudsen diffusivity, $D_{O_2,Kn}$. The dusty gas model [51] may be used to obtain the Knudsen diffusivity [52]:

$$
D_{O_2,Kn} = \frac{d_p}{3} \sqrt{\frac{8RT}{\pi M_{O_2}}}
\tag{3}
$$

where d_p is the pore diameter, R is universal gas constant, T is the local temperature, and M_{O_2} is the molecular weight of oxygen. In this study, we used the average pore diameter for d_p in Equation (3) since Lange et al. [9] showed negligible difference in calculated effective diffusivities when average and local pore diameters were assumed. The effective, local scale oxygen diffusivity in air, $D_{O_2}^{a}$, is obtained using the Bosanquet equation [53] as:

$$
D_{O_2}^{a} = \left(\frac{1}{D_{O_2-N_2}} + \frac{1}{D_{O_2,Kn}} \right)^{-1}
\tag{4}
$$

The rate of oxygen consumption in Equation (1), J_{O_2}, may be obtained using Tafel Equation [54] as:

$$
J_{O_2} = -\frac{1}{4F} i_0 \frac{c_{O_2}^{r}}{c_{O_2}^{ref}} \exp\left(\frac{-\alpha_c F}{RT} \eta \right)
\tag{5}
$$

where F is Faraday's constant, $c_{O_2}^{r}$ is the oxygen concentration at the reaction site which is calculated by oxygen transport equation, $c_{O_2}^{ref}$ is the reference oxygen concentration value at standard temperature and pressure (1 atm and 298 °K), i_0 is exchange current density, α_c is the transfer coefficient of cathode, and η is the overpotential in CCL. As mentioned earlier, constant overpotential along the CCL was assumed [55] equal to 0.4 [9]. Since the investigation of electron and proton transports in CCL was not in the scope of this study,

it was assumed that proton and electron conductivities of the CCL are large enough to ensure the available proton and electron concentrations at the reaction sites. However, this assumption leads to an overestimation of oxygen consumption rates due to neglecting the barriers against proton transport. Table 1 shows the values of parameters in Equation (5) and physical parameters used in this study. Applying the units of parameters according to Table 1 the unit of J_{O_2} is [mol.m^{-3}.s^{-1}].

Reduction of 1 mol oxygen in the electrochemical reactions produces 2 mol water and the flux of water production, J_{H_2O}, can be obtained as follows:

$$J_{H_2O} = -2J_{O_2} \tag{6}$$

To obtain the distribution of the produced water in CCL, two equations were solved: a momentum equation that includes surface tension force, and a continuity equation. The momentum equation may be written as:

$$\underbrace{\frac{\partial(\rho \boldsymbol{U})}{\partial t} + \boldsymbol{\nabla}.(\rho \boldsymbol{UU})}_{\text{inertial forces}} - \underbrace{\boldsymbol{\nabla}.(\mu \boldsymbol{\nabla U})}_{\text{viscous forces}} - \underbrace{\rho \boldsymbol{g}}_{\text{gravity forces}}$$

$$= - \underbrace{\boldsymbol{\nabla}p}_{\text{pressure forces}} - \underbrace{\boldsymbol{F}_{\text{s}}}_{\text{surfce tension forces}} \tag{7}$$

where $\boldsymbol{U}$ is the local fluid velocity, ρ is fluid density, μ is viscosity, p is local pressure, and $\boldsymbol{F}_{\text{s}}$ is the surface tension force, which is applied at the phase interfaces. The continuity equation takes the form:

$$\boldsymbol{\nabla}.\boldsymbol{U} = 0 \tag{8}$$

Applying a macroscopic-modelling methodology on gas diffusion layer and microporous layer, Weber [60] showed that the convection process through the diffusion medium does not cause high saturation changes to considerably affect gas-phase diffusion. However, given the CCL's small pore sizes, the interfacial forces strongly control the location of phase interfaces, and, subsequently, the trajectory of pathways for transport of oxygen.

Flow of the liquid water was simulated by applying the volume of fluid (VOF) method which has been used in several studies for micro- and nanoscale two-phase problems [48,61–64]. Equations (7) and (8) for this purpose were solved in order to obtain the liquid phase volume, F_v, in each cell of the imposed numerical grid, such that $F_v = \alpha V_{\text{cell}}$, where V_{cell} is the cell volume. The value of α will be one and zero for completely saturated and dry cells, respectively, and between zero and one at phase interfaces [65]. The movement of interfaces is calculated by solving a transport equation for α as:

$$\frac{\partial \alpha}{\partial t} + \boldsymbol{\nabla}.(\boldsymbol{U}\alpha) + \boldsymbol{\nabla}.(\alpha(1-\alpha)\boldsymbol{U}_r) = 0 \tag{9}$$

where $\boldsymbol{U}$ is the velocity of the two-phase flow. The last term of

Equation (9) is applied at the interface. This term represents a compression term as suggested by Weller [66] in order to minimize dispersion of the interface. $\boldsymbol{U}_r$ can be calculated as:

$$\boldsymbol{U}_r = c_r|\boldsymbol{U}| \frac{\boldsymbol{\nabla}\alpha}{|\boldsymbol{\nabla}\alpha|}$$

The parameter c_r controls the compression of the interface. Following Weller [66], the value of c_r was taken within the range of $1 \leq c_r \leq 4$ in order to obtain a sharp interface. The fluid properties used in Equations (1) and (7) were obtained by volume averaging the properties of fluids in each numerical cell.

2.2. Pore scale model

A CCL is consisted of agglomerates of carbon particles covered by platinum particles in presence of ionomer. Addition of PTFE particles imposes hydrophobic conditions of the solid surfaces. In this study, uniform distributions of platinum and PTFE particles were considered at the surface of agglomerates [9]. Oxygen, ionomer, and carbon covered by platinum particles make a three-phase region over which the electrochemical reactions occur. Oxygen in CCL diffuses through the pore spaces to reach to the reaction sites. The product of electrochemical reactions, mainly liquid water [31], creates a barrier against oxygen transport to reach to the three-phase region.

To create a pore structure of CCL we considered a section of this layer situated close to the GDL. The agglomerates were assumed as spherical solids which were randomly placed within the domain with the maximum overlap of 20% of the agglomerate's radius [9]. An agglomerate diameter of 100 nm was chosen which is reported by several studies [48,67,68], and has been found as the optimum value for the agglomerate size [12].

2.3. Simulation procedure

The discretised form of governing equations was solved using OpenFOAM software [64,69] which applies the finite volume method. Solution of Equation (1) provided oxygen concentration throughout the domain including the reaction sites where the water production at the agglomerates was calculated. When the molar ratio of the liquid water in each numerical grid cell reached a value of one we considered that local numerical cell as water saturated. Fig. 1b provides a schematic part of numerical domain used in our simulation, showing production of water in the cells adjacent to the surface of agglomerates where reaction occurs. The cell size of the computational domain was chosen small enough to have an initial saturation value of less than 0.10 if all cells adjacent to the agglomerates become water saturated.

Solving the two-phase flow and reactive solute transport at each time step of water production can be extremely time consuming due to small time steps needed for the numerical stability. As such, we have applied a sequential approach using which when the number of water saturated cells, due to electrochemical relations, reached to a defined threshold number the two-phase flow equations were solved. The value of threshold number should be small enough to have negligible effect on the final water distribution. To do so, we have performed several simulations to find a value of the threshold number which has negligible effect on water distribution. We found that choosing the value of the threshold number equal to 25% of the number of the remaining dry cells neighbour to the surface of agglomerates results in accurate calculation of water distribution. Applying this condition, after solving the two-phase flow problem at each step, Equation (1) was solved for calculation of solute propagation and electrochemical reactions. For boundary

Table 1
Parameters used in simulations.

Property	Value
T (K)	353
p (atm)	1
α_c	0.61 [56]
i_0 (A.m^{-2})	1.659×10^{-2} [56]
η (V)	0.4 [17]
$c_{O_2}^{\text{ref}}$ (mol.m^{-3})	40.96
$D_{O_2-N_2}$ (m^2.s^{-1})	2.75×10^{-5} [57]
$D_{O_2}^{\text{w}}$ (m^2.s^{-1})	6.395×10^{-9} [58]
$H_{O_2}^{\text{cc}}$	42.785 [59]

conditions in two-phase flow simulation, the surfaces of agglomerates were assumed as solid surfaces with specific contact angles and symmetry condition were applied for the rest of boundaries. The effect of this boundary condition on the results will be discussed later in Section 3.5. For transport of oxygen the inlet concentration (i.e., at the interface between CCL and GDL) was assigned with a value equal to oxygen concentration ratio in air at the operating conditions in the unit of $[mol.m^{-3}]$ while symmetry condition was assumed for other boundaries.

To explore the wettability effects on performance of CCL, simulations were performed by applying two different contact angles at the surface of agglomerates. While a value of contact angle below 90 represents a hydrophilic surface, a value larger than 90 creates hydrophobic surfaces (Fig. 1a). Wettability changes have different effects on the resulting water distribution in CCL due to presence of pores with different sizes. In the hydrophobic domain, water imbibes into the larger pores and blocks oxygen pathways and decreases oxygen diffusive flux through the porous media. However, at the same time, hydrophobicity will cause water to have less affinity towards the solid surfaces and covers a lower fraction of reaction surface areas at the agglomerates where electrochemical reactions may occur. In contrast, hydrophilic surfaces increase wettability and cause a larger fraction of reaction surface areas to be covered by the liquid water. At the same time, the water in the hydrophilic domain spreads over the surface of agglomerates where the center of pores may remain air-filled, letting oxygen to diffuse faster through these pathways.

3. Results and discussion

In this study, the value of effective diffusivity (i.e., the integrated diffusivity of the whole domain) was obtained under a wide range of water saturation levels. To do so, during the flow/transport/reaction simulation procedure, at several stages with different saturation levels, we have taken the resulting air and water distributions to perform a tracer transport through the domain. Having the distribution of air and water in the domain, the boundary concentration of tracer (non-reacting oxygen) was set as fixed values at the inlet and the opposite boundary and Equation (1) was solved to reach the steady-state form to obtain the flux of oxygen across the whole domain. Clearly, for the tracer transport simulation no electrochemical reactions were included. The calculated steady-state flux of solute at the outlet, Γ_{out}, was used to obtain the normalized effective diffusivity, D, as:

$$D = \frac{L}{A} \frac{\Gamma_{out}}{D_{O_2-N_2}(c_1 - c_2)} \qquad (10)$$

where c_1 and c_2 are the applied tracer molar ratios at the inlet and outlet boundaries, L is the total length of the domain, and A is the total boundary area including pores and solids. To obtain a representative domain size, we have performed several simulations using different cubic domains with different sizes to obtain the domain size needed for calculation of diffusivity values as shown in Fig. 2. A convergence is achieved by choosing a domain with the size of $1.0 \times 1.0 \times 1.0 \ \mu m^3$ where the variation of results is less than 2%.

3.1. Model validation

Simulation results of diffusivity are often validated against the results from the Bruggeman correlation [9]. Bruggeman relation [24] describes tortuosity as $\tau = \varepsilon^{1/2}$, where ε is the porosity. Tortuosity may be correlated to the normalized effective diffusivity, D, through the expression $D = \varepsilon/\tau$ [70]. Substituting the Bruggeman
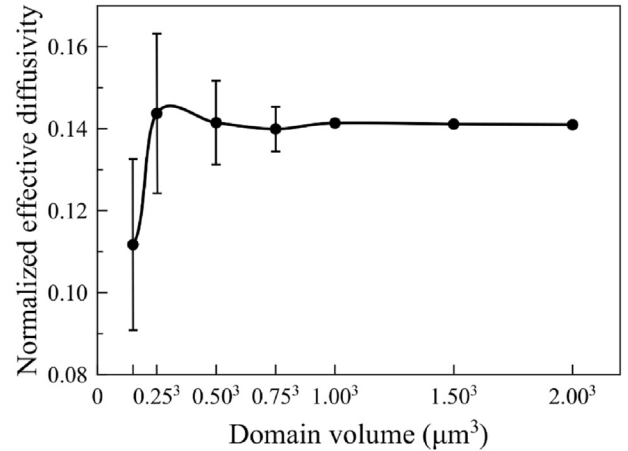

Fig. 2. The effect of domain size on normalized effective diffusivity. The simulations were made for the cubic domains with the porosity of about 0.54.

relation into the effective diffusivity expression provides $D = \varepsilon^{3/2}$. This equation is known as Bruggeman correlation for effective diffusivity [9]. Moreover, Bruggeman conducted several experiments using porous domain composed of uniformly spaced, equally-sized, solid spheres [24]. The porosity of such a media can be estimated as $(1 - \pi/6)$, regardless of sphere diameters. This conditions leads to $D = (1 - \pi/6)^{3/2} \approx 0.3288$. Table 2 shows the normalized effective diffusivities of the domain consisting of different numbers of grains which were uniformly spaced as well as the normalized effective diffusivity obtained by the Bruggeman experiment. It can be observed that the simulation results are in good agreement with the result of Bruggeman experiment. We have found similar range of differences as those reported by Lange et al. [9]. This slight difference between the results may be due to the use of structured mesh which results in less accuracy in representing spherical surfaces.

We also compared the simulation results under the dry conditions with the results reported by Lange et al. [9]. Lange et al. calculated the effective diffusivity of oxygen in a CCL composed of several equally-sized carbon particles with the diameter of 24 nm in a domain with the size of $200 \times 200 \times 200 \ nm^3$ and the maximum pore volume fraction of less than 0.5. Each carbon particle was covered by ionomer with fixed thickness of 4 nm. We applied the diameter of 32 nm for spheres in a bigger domain with the size of $320 \times 320 \times 320 \ nm^3$ to compare our results with the results of Lange et al. model under the same condition. In our simulations, we considered the ionomer domain as part of the carbon particle since Lange et al. [9] assigned oxygen diffusivity of ionomer four orders of magnitude smaller compared with diffusivity in air which applies a strong hindering effect. The comparison provided in Fig. 3 indicates the agreement between the results for the normalized effective diffusivity under two conditions — i.e., including and excluding the Knudsen effect. Fig. 3 shows the

Table 2
Simulation results for the domain consisting of uniformly spaced spheres and comparison with the Bruggeman correlation.

Number of spheres	Porosity	D
1	0.4760	0.3378
8	0.4740	0.3293
27	0.4756	0.3230
64	0.4756	0.3225
125	0.4767	0.3204
Bruggeman	0.4764	0.3288
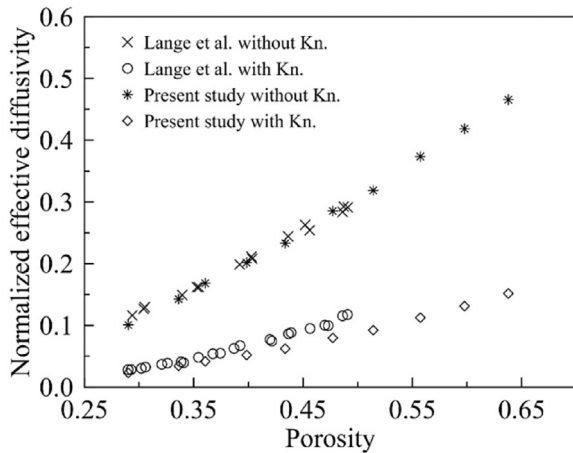
Fig. 3. Comparison of normalized effective diffusivity obtained using our model with the results reported by Lange et al. [9] for porosity values up to 0.50. To have identical Knudsen effect, agglomerates of equal sizes with the study of Lange et al. have been used.

importance of Knudsen effect on the effective diffusivity due to the presence of nano-pores in CCL [71].

3.2. Effective diffusivity calculations

The distribution of the produced liquid water was obtained for different water saturation levels in the domain with the porosity of 0.55. Nearly, the same porosity value was observed for the real structure of CCL obtained using FIB/SEM experiments [41]. Fig. 4 provides water distribution under several different saturation levels in hydrophilic and hydrophobic domains represented by the contact angles of 20 and 150, respectively. Water in the

hydrophobic domain is considered as the non-wetting phase while it is the wetting phase in hydrophilic media. Water distribution for this reason is considerably different in the domains with different wettabilities. Fig. 4 shows the different pore scale water distributions for the two domains with different wettabilities. Water invades into the pores in hydrophobic domain and accumulates within the bulk space of these pores. On the other hand, water remains close to the surface of agglomerates and films of water are created in hydrophilic domain. Hutzenlaub et al. [41], assumed water as spherical objects in both hydrophilic and hydrophobic domains. Fig. 4 shows that this assumption may not be accurate as the water in the hydrophilic domain is presented mostly as thin films at the surface of agglomerates. Moreover, they assumed that water in the hydrophobic domain occupies only the largest pores. Solving the two-phase flow equations shows that, particularly at the low saturation level (Fig. 4a and d), some larger pores are not filled by the liquid water. Therefore, neglecting the two-phase flow dynamics and assuming that the larger pores are filled by water may underestimate the invasion of water into smaller pores. The presence of air-filled larger pores in hydrophobic domain while some smaller pores are water-filled can happen due to the water production in the entire domain and the local invasion of water to the adjacent pores.

Water in hydrophobic domain preferentially accumulates and fills the large pore spaces which causes blockage of pores and hinders the diffusion of oxygen through the domain. In contrast, water remains close to the agglomerate surfaces and distributes over larger fraction of surface areas in the hydrophilic domain. Hence, pores may not be completely filled by water and presence of air pathways is more likely in comparison with the hydrophobic domain at the same saturation levels.

The effect of wettability on water distribution can be shown by analyzing the size of pores which are occupied by water at different saturation levels. We have calculated the pore size distribution of water-filled pores for both hydrophilic and hydrophobic domains at
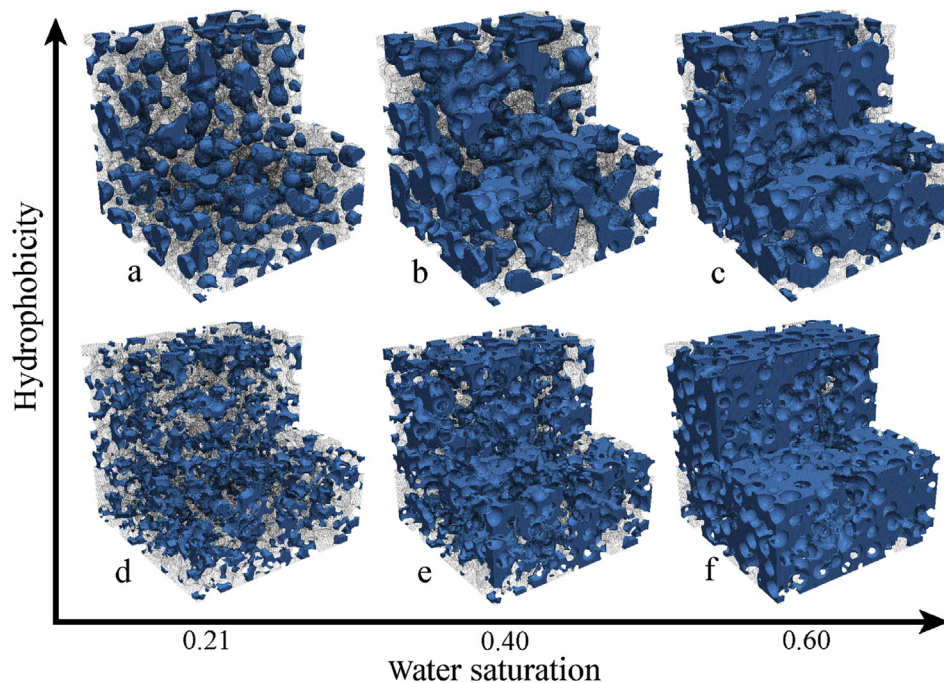
Fig. 4. Effect of hydrophobicity on liquid water distribution within the pore spaces. The hydrophilic domain has a contact angle of 20, and the hydrophobic domain has a contact angle of 150. The porosity is 0.55 and the saturation values, S, are 0.21 in (a) and (d), 0.40 in (b) and (e), and 0.60 in (c) and (f). The computational domain is shown in gray with a reduced opacity and water is shown in blue. (For interpretation of the references to colour in this figure legend, the reader is referred to the web version of this article.)
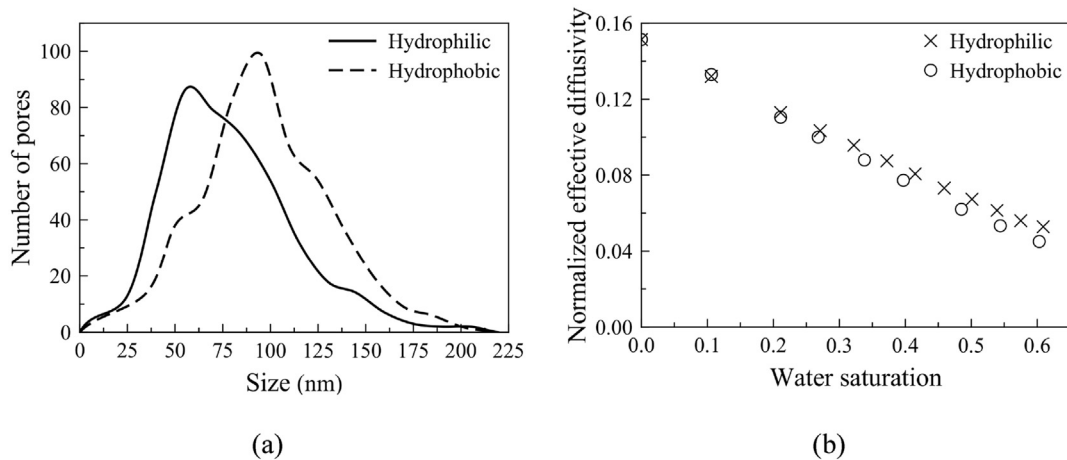
Fig. 5. a) The volumetric pore size distribution of water-filled pores for hydrophilic and hydrophobic domains at the saturation value of 0.40. b) The effect of water saturation on normalized effective diffusivity values.

the saturation of 0.4 which is shown in Fig. 5a. The size distribution was obtained applying the watershed based algorithm using Avizo image analysis (FEI, USA) [72] on the numerical results. The water-filled pore size distributions confirm that a higher fraction of larger pores in the whole domain are filled with water for the hydrophobic domain, although a fraction of smaller pores is also invaded by water. Consequently, a reduced number of pathways are available for gas in the hydrophobic domain and higher effective diffusivity values are expected for the hydrophilic media.

To obtain the effective diffusivity of the domain, tracer transport was performed under different saturation levels for both hydrophilic and hydrophobic domains. We should note that, three realizations were performed for every case, each by setting c_1 and c_2 in Equation (10) normal to one of the three orthogonal directions (x, y, and z). We have found approximately equal results for tracer transport in different directions. Fig. 5b indicates how water saturation affects the normalized effective diffusivity. For different saturation levels, the effective diffusivity of the hydrophilic domain indicates higher diffusivity values which can be explained based on the presence of gas flow pathways explained in our observations in Figs. 4 and 5a. It is clear from Fig. 5b that the increase of saturation level decreases the normalized effective diffusivity in both domains approximately linearly up to the saturation value of 0.60.

Calculating the cross-sectional area of the air-filled pores in slices located at different distances, and perpendicular to the direction of oxygen diffusion, roughly same cross-sectional area was obtained for both hydrophilic and hydrophobic domains. This similarity together with the possible effect of using a mean pore diameter to calculate Knudsen diffusivity may explain our observation of comparable effective diffusivity for both hydrophilic and hydrophobic domains. Slightly higher values of air-filled pores area were obtained in hydrophilic domain which causes higher values for normalized effective diffusivity in this domain compared to the hydrophobic CCL as is shown in Fig. 5b. Hutzenlaub et al. [41] also reported that hydrophilic and hydrophobic domains have nearly the same values of effective diffusivity. They did not solve the two-phase flow problem and assumed that all small pores are occupied by water and less number of pathways for oxygen transport was available in partially-saturated hydrophilic domain and more number of pathways was available in partially-saturated hydrophobic domain. Hence, using their method, an underestimation and an overestimation may happen in the calculation of the effective diffusivity values in hydrophilic and hydrophobic domains, respectively. The resulted effective diffusivity obtained by

their model in hydrophobic domain was higher than that in hydrophilic media, in particular at high saturation levels. This is in contrast with the results shown in Fig. 5b.

3.3. Agglomerate covering effect by the liquid water

So far, we have shown the effect of water saturation on transport of oxygen. After transport of oxygen and its ultimate arrival at the reaction sites, the subsequent electrochemical reaction depends on the availability of reaction surfaces and whether these surfaces are dry or covered by the liquid water. To explore this effect, we have calculated the fraction of dry surface area of agglomerates as saturation increases for both hydrophilic and hydrophobic domains. Fig. 6a shows the decrease of available reaction surface area by increasing saturation level under different contact angles. A parabolic curve is also fitted to the numerical results which is shown in Fig. 6a. It is clear that wettability has a significant effect of evolution of reaction surface area which decreases non-linearly with increasing saturation. For example, at a saturation value of 0.6, the hydrophobic domain has about two times larger amount of available reaction surface area compared to the hydrophilic domain which can be observed in Table 3 as well. In this aspect, our results show a similar trend to the results obtained by Hutzenlaub et al. [41]. However, they reported larger differences between the available surface areas from hydrophilic and hydrophobic domains. This can be due to their assumption that water can occupy largest and smallest pores in the entire hydrophobic and hydrophilic domains, respectively. This assumption leads to an overestimation and an underestimation of available surface area in hydrophobic and hydrophilic domains, respectively.

As water in hydrophilic domain preferentially covers the agglomerate surfaces, rather than filling the bulk pore spaces, flooding may happen at lower saturation levels in hydrophilic domains compared to the hydrophobic media. Applying a parabolic curve fitting on the results, it can be approximated that there is no available surface area when saturation levels of the hydrophilic and hydrophobic domains reach to values of 0.71 and 0.94, respectively (Table 3). Therefore, the fuel cell with hydrophobic CCL may operate at high saturation levels in the absence of liquid water removal. Similar effect has been observed by Hutzenlaub et al. [41].

3.4. Oxygen consumption rate

The combined effect of the two rate-controlling mechanisms
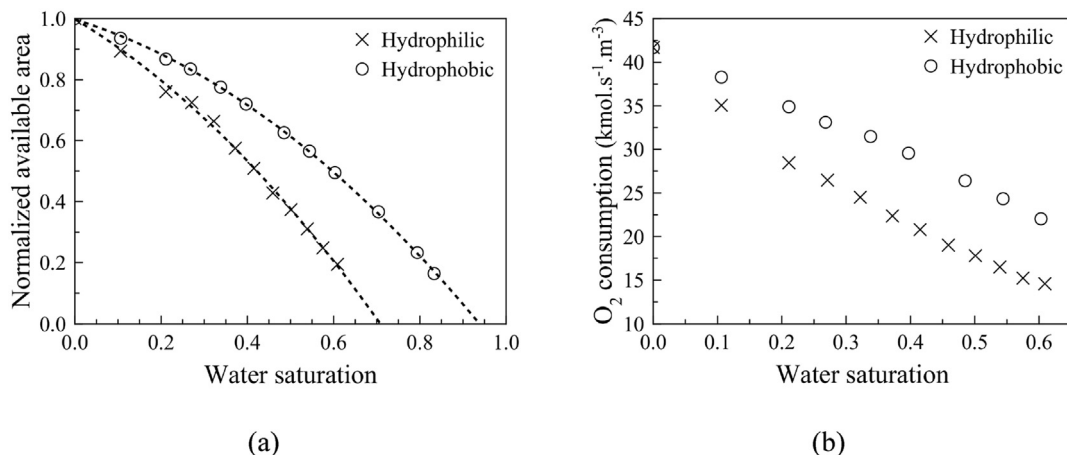
Fig. 6. a) The covering effect of water saturation on the available surface area. Vertical axis shows available surface area normalized by the total surface area of the agglomerates. Dashed lines show the fitted curves to the simulation results. b) The effect of saturation on decrease of oxygen consumption rate.

Table 3
The dry portion of agglomerate surfaces, not covered by liquid water, in hydrophilic and hydrophobic domains at different saturation levels.

Saturation	Dry fraction of agglomerates surfaces	
	Hydrophilic	Hydrophobic
0.00	1.00	1.00
0.10	0.89	0.94
0.21	0.76	0.87
0.40	0.54	0.71
0.60	0.21	0.50
0.71[a]	0.00	0.36
0.94[a]	0.00	0.00

[a] Predicted by using the curve fits in Fig. 6a.

(i.e., transport of oxygen along the media and coverage of reaction surface areas) will determine the ultimate rate of oxygen consumption. The change of oxygen consumption versus the saturation is shown in Fig. 6b.

It can be observed that the hydrophobic domain has higher oxygen consumption rate owing to the presence of larger amount of available surface area. This shows that a hydrophobic CCL can increase the performance of the cell which is in agreement with the experimental results [42]. It should be noted that, however, due to neglecting the barriers against proton and electron transports in this study, the absolute values of oxygen consumption rate provided in Fig. 6b are likely to be overestimated [19].

3.5. Water removal condition

In this section, we evaluate the assumption of considering symmetry flow boundary conditions which enabled us to reach a wide range of water saturations, however, at the cost of preventing water removal. When assigning open boundaries for hydrophobic CCL, a fraction of water leaves the domain from the surrounding domain boundaries and the remaining water will be mostly trapped within the larger pores. The amount of remained water determines the final saturation of CCL. The final saturation can be obtained when CCL reaches to a steady state condition under which the amount of the produced water is equal to the amount removed from the open boundaries, resulting in a fixed, time independent, value of saturation. To investigate this effect, a constant pressure value was assumed for the surrounding boundaries and the contact angle of 150 was assigned for the surface of agglomerates. The simulations were continued to reach the final steady-state

saturation. As simulation proceeds, the produced water leaves the domain due to the hydrophobicity, and the reaction sites become available helping the continuation of water production.

The final water distribution for a domain with the contact angle of 150 is provided in Fig. 7. It can be seen in Fig. 7a that due to the hydrophobicity of the surfaces, a fraction of the liquid water leaves the domain while the rest moves into the larger pore spaces. Therefore, more surface area of agglomerates is made available for the electrochemical reactions. Fig. 7b shows a two-dimensional slice through middle of the domain. It can be observed that the liquid water occupies the largest pores of the domain. Some small pores, mostly located between the large pores, are also occupied by the liquid water. However, much of the small pores are air-filled through which oxygen can diffuse.

We evaluated the effect of boundary conditions on oxygen transport and available reaction surface area. The resulted effective diffusivity and available surface area obtained by assuming closed and open boundaries for a domain with the contact angle of 150 are shown in Fig. 8a and b, respectively, up to the final achievable saturation values for the open domain. Fig. 8 shows that the closed boundary type overestimates the diffusivity and available surface area values, however the effects are not large. Although use of an open boundary conditions would have resulted in slightly more exact simulations, the effective diffusivity and available surface area of the domain could be obtained only up to a saturation value of 0.28 (i.e., the final steady state saturation), limiting our analysis.

It can be observed in Fig. 8 that the final saturation of a CCL with the contact angle of 150 is about 0.28. Decreasing the contact angle causes a higher value of final saturation. Moreover, during the operation of CCL in a PEMFC the final saturation at the equilibrium depends on the current density of the cell. Using the results provided in Figs. 5b and 6a, the effective diffusivity and available area of the CCL can be estimated having the knowledge of final saturation related to a specific current density of fuel cell. For example, increasing the current density which results in the final saturation of 0.6 in a hydrophobic CCL having contact angle of 150 causes the decrease of available reaction area up to 50%. Under this condition, most of the platinum particles cannot participate in the electrochemical reactions and hence the performance of CCL decreases. Moreover, the effective diffusivity of a CCL working at high saturation levels is much less than that of a CCL operating at lower saturation levels. Therefore, the oxygen concentration decreases along the depth of CCL towards the proton exchange membrane. This condition leads to lower oxygen consumption rates along the

(a)   (b)
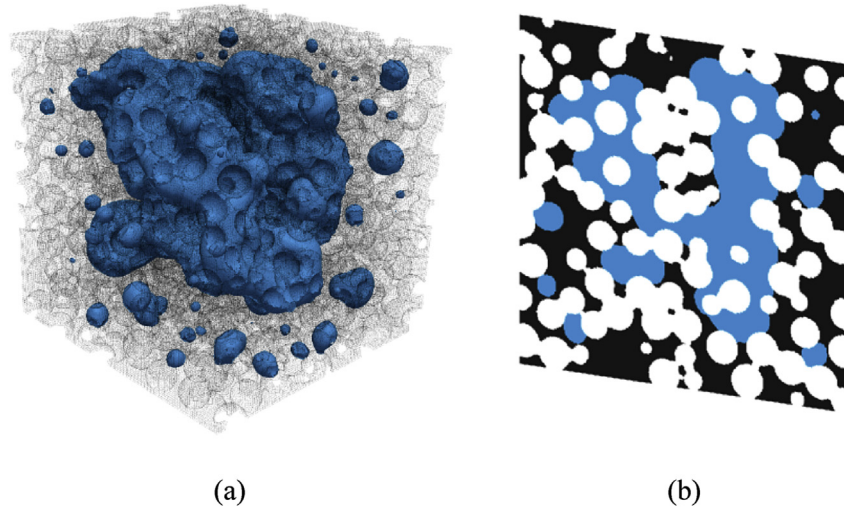
Fig. 7. Water distribution for a hydrophobic domain with the contact angle of 150 and the porosity of 0.55. The figure shows the domain at the final saturation of 0.28 in (a) while the computational grid is shown in grey with opacity and water is shown in blue. The figure shows a middle slice of the domain in (b). The liquid water is in blue, the pore spaces are in black and the agglomerates are in white. (For interpretation of the references to colour in this figure legend, the reader is referred to the web version of this article.)

(a)   (b)
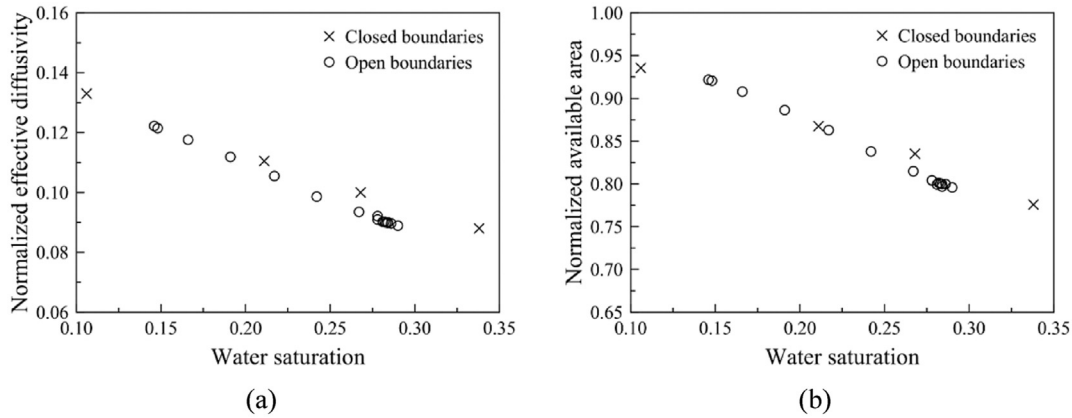
Fig. 8. a) The normalized effective diffusivity and b) the normalized available area of the hydrophobic domain with open and closed boundary conditions. The contact angle and the porosity of the domains are 150 and 0.55, respectively.

depth of the CCL as well as less electrochemical reaction rate which decreases the performance of CCL.

4. Conclusion

Operation of PEMFC creates liquid water, an undesired process that decreases the performance of the fuel cell. This is because the produced liquid water affects both gas transport through the pore spaces of the CCL and reaction processes taking place at the agglomerate solid surfaces. In the present study, we have developed a pore-scale model to assess the effect of produced liquid water distributions on effective diffusivity and available reaction surface area under different contact angles. A key feature of the model is that it considered the three main processes of two-phase flow, solute transport, and electrochemical reactions to simulate diffusivity of CCL. Consumption of oxygen by the electrochemical reactions caused production of the liquid water and the subsequent two-phase flow of water through the pore spaces. To represent the hydrophilic and the hydrophobic wettability effects, simulations were performed using different contact angles. The normalized effective diffusivity values were obtained for each condition. We found that:

- The occupation of larger pore spaces by water blocks the hydrophobic domain and lowers the effective diffusivity more than that observed for the hydrophilic domain. Alternatively, the coverage of reaction surface areas by the liquid water is strong under hydrophilic conditions. A domain with the contact angle of 150 showed to have nearby twice available surface area than a domain with the contact angle of 20 for the same saturation value of 0.60.

- A complete flooding happens in hydrophilic and hydrophobic CCLs when the saturation reaches about 0.71 and 0.94, respectively. The responsible mechanism for flooding in the hydrophilic CCL at lower saturation level is the tendency of water to stay adjacent to the hydrophilic surfaces. The hydrophobic condition of CCLs assists to maintain a higher fraction of available reaction surface area as well as more efficient removal of water from the media.

- Due to having more available reaction area, the hydrophobic CCL has higher oxygen consumption rate which can increase the performance of the cell. However, the amount of hydrophobicity affects the proton conductivity of CCL which may be considered in future works.

- The effects of water removal on the effective diffusivity as well as the available area of the hydrophobic domain were investigated. It was found that the assumption of closed boundaries for CCL, which prevents water to leave the domain, has no significant effect on the resulting effective diffusivity values. The major consequence of no water removal is on the final achievable saturation of the domain which affects the fuel cell operation. We found that the final saturations of the hydrophobic CCL with the contact angle of 150 are 0.94 and 0.28 when the boundaries are closed and open, respectively.

- Higher saturation values in the domain with closed boundaries diminished available surface area which implies that the fuel cell does not operate at these saturations. However, for the domain with open boundaries, fuel cell continues its operation under a constant saturation level as a large fraction of surface area remains available for the electrochemical reactions.

In present study, the evaporation of liquid water in CCL was neglected. Since the initial evaporation rate of water is much faster than the capillary flow [31], this assumption is expected to be appropriate. The gas phase in the pore spaces becomes saturated with water vapor in a short time scale, which sets the net evaporation rate of water to zero. This study considered agglomerates with ideal, spherical shapes. Application of CCL's real structure as well as the effect of applying different contact angles or mixed wettability on the final saturation should be investigated in future studies.

References

[1] Fuel Cell Technologies Market Report 2015, 2016. http://energy.gov/sites/prod/files/2015/10/f33/fcto_2015_market_report.pdf (accessed 21 February 2017).

[2] T.E. Springer, M.S. Wilson, S. Gottesfeld, Modeling and experimental diagnostics in polymer electrolyte fuel cells, J. Electrochem. Soc. 140 (1993) 3513—3526.

[3] T.E. Springer, T. Zawodzinski, S. Gottesfeld, Polymer electrolyte fuel cell model, J. Electrochem. Soc. 138 (1991) 2334—2342.

[4] E. Ticianelli, J. Beery, S. Srinivasan, Dependence of performance of solid polymer electrolyte fuel cells with low platinum loading on morphologic characteristics of the electrodes, J. Appl. Electrochem. 21 (1991) 597—605.

[5] M. Eikerling, A. Kornyshev, Modelling the performance of the cathode catalyst layer of polymer electrolyte fuel cells, J. Electroanal. Chem. 453 (1998) 89—106.

[6] Z.N. Farhat, Modeling of catalyst layer microstructural refinement and catalyst utilization in a PEM fuel cell, J. Power Sources 138 (2004) 68—78.

[7] F.C. Cetinbas, S.G. Advani, A.K. Prasad, A modified agglomerate model with discrete catalyst particles for the PEM fuel cell catalyst layer, J. Electrochem. Soc. 160 (2013) F750—F756.

[8] P.P. Mukherjee, C.-Y. Wang, Modeling of catalyst layer surface coverage and volume blockage owing to liquid water in a PEFC, ECS Trans. 3 (2006) 1085—1094.

[9] K.J. Lange, P.-C. Sui, N. Djilali, Pore scale simulation of transport and electrochemical reactions in reconstructed PEMFC catalyst layer, J. Electrochem. Soc. 157 (2010) B1434—B1442.

[10] P. Dobson, C. Lei, T. Navessin, M. Secanell, Characterization of the PEM fuel cell catalyst layer microstructure by nonlinear least-squares parameter estimation, J. Electrochem. Soc. 159 (2012) B514—B523.

[11] R. Singh, A. Akhgar, P. Sui, K. Lange, N. Djilali, Dual-beam FIB/SEM characterization, statistical reconstruction, and pore scale modeling of a PEMFC catalyst layer, J. Electrochem. Soc. 161 (2014) F415—F424.

[12] T. Sousa, C. Rangel, Pore scale modelling of a cathode catalyst layer in fuel cell environment: agglomerate reconstruction and variables optimization, J. Solid State Electrochem. 20 (2016) 541—554.

[13] K.J. Lange, P.-C. Sui, N. Djilali, Pore scale modeling of a proton exchange membrane fuel cell catalyst layer: effects of water vapor and temperature, J. Power Sources 196 (2011) 3195—3203.

[14] M. El Hannach, J. Pauchet, M. Prat, Pore network modeling: application to multiphase transport inside the cathode catalyst layer of proton exchange membrane fuel cell, Electrochim. Acta 56 (2011) 10796—10808.

[15] D.M. Bernardi, M.W. Verbrugge, A mathematical model of the solid-polymer-electrolyte fuel cell, J. Electrochem. Soc. 139 (1992) 2477—2491.

[16] C. Marr, X. Li, Composition and performance modelling of catalyst layer in a proton exchange membrane fuel cell, J. Power Sources 77 (1999) 17—27.

[17] J. Baschuk, X. Li, Modelling of polymer electrolyte membrane fuel cells with variable degrees of water flooding, J. Power Sources 86 (2000) 181—196.

[18] S. Mazumder, J.V. Cole, Rigorous 3-D mathematical modeling of PEM fuel cells I. Model predictions without liquid water transport, J. Electrochem. Soc. 150 (2003) A1503—A1509.

[19] Q. Wang, M. Eikerling, D. Song, Z. Liu, Structure and performance of different types of agglomerates in cathode catalyst layers of PEM fuel cells, J. Electroanal. Chem. 573 (2004) 61—69.

[20] D. Song, Q. Wang, Z. Liu, T. Navessin, S. Holdcroft, Numerical study of PEM fuel cell cathode with nonuniform catalyst layer, Electrochim. Acta 50 (2004) 731—737.

[21] N. Khajeh-Hosseini-Dalasm, M. Kermani, D.G. Moghaddam, J. Stockie, A parametric study of cathode catalyst layer structural parameters on the performance of a PEM fuel cell, Int. J. Hydrogen Energy 35 (2010) 2417—2427.

[22] M. Tohidi, S.H. Mansouri, H. Amiri, Effect of primary parameters on the performance of PEM fuel cell, Int. J. Hydrogen Energy 35 (2010) 9338—9348.

[23] W. Henry, Experiments on the quantity of gases absorbed by water, at different temperatures, and under different pressures, Phil. Trans. R. Soc. B 93 (1803) 29—276.

[24] V.D. Bruggeman, Berechnung verschiedener physikalischer Konstanten von heterogenen Substanzen. I. Dielektrizitätskonstanten und Leitfähigkeiten der Mischkörper aus isotropen Substanzen, Ann. Phys. 416 (1935) 636—664.

[25] G. Hu, G. Li, Y. Zheng, Z. Zhang, Y. Xu, Optimization and parametric analysis of PEMFC based on an agglomerate model for catalyst layer, J. Energy Inst. 87 (2014) 163—174.

[26] V. Gurau, H. Liu, S. Kakac, Two-dimensional model for proton exchange membrane fuel cells, AIChE J. 44 (1998) 2410—2422.

[27] L. You, H. Liu, A two-phase flow and transport model for the cathode of PEM fuel cells, Int. J. Heat. Mass Transf. 45 (2002) 2277—2287.

[28] Z. Wang, C. Wang, K. Chen, Two-phase flow and transport in the air cathode of proton exchange membrane fuel cells, J. Power Sources 94 (2001) 40—50.

[29] J.H. Nam, M. Kaviany, Effective diffusivity and water-saturation distribution in single-and two-layer PEMFC diffusion medium, Int. J. Heat. Mass Transf. 46 (2003) 4595—4611.

[30] T. Berning, N. Djilali, A 3D, multiphase, multicomponent model of the cathode and anode of a PEM fuel cell, J. Electrochem. Soc. 150 (2003) A1589—A1598.

[31] G. Lin, W. He, T. Van Nguyen, Modeling liquid water effects in the gas diffusion and catalyst layers of the cathode of a PEM fuel cell, J. Electrochem. Soc. 151 (2004) A1999—A2006.

[32] D.H. Schwarz, N. Djilali, 3D Modeling of catalyst layers in PEM fuel cells effects of transport limitations, J. Electrochem. Soc. 154 (2007) B1167—B1178.

[33] P.K. Das, X. Li, Z.-S. Liu, Analysis of liquid water transport in cathode catalyst layer of PEM fuel cells, Int. J. Hydrogen Energy 35 (2010) 2403—2416.

[34] R. Friedmann, T. Van Nguyen, Optimization of the microstructure of the cathode catalyst layer of a PEMFC for two-phase flow, J. Electrochem. Soc. 157 (2010) B260—B265.

[35] L. Xing, M. Mamlouk, R. Kumar, K. Scott, Numerical investigation of the optimal Nafion® ionomer content in cathode catalyst layer: an agglomerate two-phase flow modelling, Int. J. Hydrogen Energy 39 (2014) 9087—9104.

[36] M. Eikerling, Water management in cathode catalyst layers of PEM fuel cells a structure-based model, J. Electrochem. Soc. 153 (2006) E58—E70.

[37] V. Mulone, K. Karan, Analysis of capillary flow driven model for water transport in PEFC cathode catalyst layer: consideration of mixed wettability and pore size distribution, Int. J. Hydrogen Energy 38 (2013) 558—569.

[38] P.P. Mukherjee, Q. Kang, C.-Y. Wang, Pore-scale modeling of two-phase transport in polymer electrolyte fuel cells-progress and perspective, Energy Environ. Sci. 4 (2011) 346—369.

[39] R. Alink, D. Gerteisen, Modeling the liquid water transport in the gas diffusion layer for polymer electrolyte membrane fuel cells using a water path network, Energies 6 (2013) 4508—4530.

[40] A. Raoof, S. Hassanizadeh, Saturation-dependent solute dispersivity in porous media: pore-scale processes, Water Resour. Res. 49 (2013) 1943—1951.

[41] T. Hutzenlaub, J. Becker, R. Zengerle, S. Thiele, Modelling the water distribution within a hydrophilic and hydrophobic 3D reconstructed cathode catalyst layer of a proton exchange membrane fuel cell, J. Power Sources 227 (2013) 260—266.

[42] H. Yu, C. Ziegler, M. Oszcipok, M. Zobel, C. Hebling, Hydrophilicity and hydrophobicity study of catalyst layers in proton exchange membrane fuel cells, Electrochim. Acta 51 (2006) 1199—1207.

[43] M. Uchida, Y. Aoyama, N. Eda, A. Ohta, Investigation of the microstructure in the catalyst layer and effects of both perfluorosulfonate ionomer and PTFE-loaded carbon on the catalyst layer of polymer electrolyte fuel cells, J. Electrochem. Soc. 142 (1995) 4143—4149.

[44] G.S. Avcioglu, B. Ficicilar, I. Eroglu, Effect of PTFE nanoparticles in catalyst layer with high Pt loading on PEM fuel cell performance, Int. J. Hydrogen Energy 41 (2016) 10010—10020.

[45] W. Majima, H. Matsushima, Y. Fukunaka, M. Ueda, Observation of three-phase interface during hydrogen electrode reactions in unitized regenerative fuel cell, J. Electrochem. Soc. 161 (2014) F1002—F1005.

[46] H. Matsushima, W. Majima, Y. Fukunaka, M. Ueda, In situ observation of dynamic meniscus front interface in alkaline fuel cell, ECS Electrochem. Lett. 4 (2015) F43—F45.

[47] R. Wu, Q. Liao, X. Zhu, H. Wang, Pore network modeling of cathode catalyst layer of proton exchange membrane fuel cell, Int. J. Hydrogen Energy 37 (2012) 11255—11267.

[48] H. Fathi, A. Raoof, S.H. Mansouri, M.T.v. Genuchten, Effects of porosity and water saturation on the effective diffusivity of a cathode catalyst layer,

J. Electrochem. Soc. 164 (2017) F298–F305.

[49] M.G. Mahmoodlu, N. Hartog, S.M. Hassanizadeh, A. Raoof, Oxidation of volatile organic vapours in air by solid potassium permanganate, Chemosphere 91 (2013) 1534–1538.

[50] M.G. Mahmoodlu, S.M. Hassanizadeh, N. Hartog, A. Raoof, Oxidation of trichloroethylene, toluene, and ethanol vapors by a partially saturated permeable reactive barrier, J. Contam. Hydrol. 164 (2014) 193–208.

[51] E.A. Mason, A. Malinauskas, Gas transport in Porous Media: the Dusty-gas Model, Elsevier Science Ltd, 1983.

[52] M.M. Mench, Polymer Electrolyte Fuel Cells, Fuel Cell Engines, John Wiley & Sons Inc, New York, 2008, pp. 285–379.

[53] S.H. Kim, H. Pitsch, Reconstruction and effective transport properties of the catalyst layer in PEM fuel cells, J. Electrochem. Soc. 156 (2009) B673–B681.

[54] F. Barbir, PEM Fuel Cells: Theory and Practice, Academic Press, Storrs, United States, 2012.

[55] L. You, H. Liu, A parametric study of the cathode catalyst layer of PEM fuel cells using a pseudohomogeneous model, Int. J. Hydrogen Energy 26 (2001) 991–999.

[56] A. Parthasarathy, S. Srinivasan, A.J. Appleby, C.R. Martin, Temperature dependence of the electrode kinetics of oxygen reduction at the platinum/Nafion® interface-a microelectrode investigation, J. Electrochem. Soc. 139 (1992) 2530–2537.

[57] E.N. Fuller, P.D. Schettler, J.C. Giddings, Diffusion of halogenated hydrocarbons in helium. The effect of structure on collision cross sections, Ind. Eng. Chem. 58 (1966) 18–27.

[58] W. Hayduk, H. Laudie, Prediction of diffusion coefficients for nonelectrolytes in dilute aqueous solutions, AIChE J. 20 (1974) 611–615.

[59] J.C. Amphlett, R. Baumert, R.F. Mann, B.A. Peppley, P.R. Roberge, T.J. Harris, Performance modeling of the Ballard Mark IV solid polymer electrolyte fuel cell I. Mechanistic model development, J. Electrochem. Soc. 142 (1995) 1–8.

[60] A.Z. Weber, Improved modeling and understanding of diffusion-media wettability on polymer-electrolyte-fuel-cell performance, J. Power Sources 195 (2010) 5292–5304.

[61] D. Banerjee, Investigation of volume of fluids (VOF) method and system models for design of microfluidic ink delivery apparatus for dip pen nano-lithography (DPN), NSTI Nanotech (2005) 10–12.

[62] A. Bedram, A. Moosavi, Breakup of droplets in micro and nanofluidic T-junctions, J. Appl. Fluid Mech. 6 (2013) 81–86.

[63] A. Bedram, A. Moosavi, S.K. Hannani, A novel method for producing unequal sized droplets in micro-and nanofluidic channels, Eur. Phys. J. E 38 (2015) 1–9.

[64] N.K. Palakurthi, S. Konangi, U. Ghia, K. Comer, Micro-scale simulation of unidirectional capillary transport of wetting liquid through 3D fibrous porous media: estimation of effective pore radii, Int. J. Multiph. Flow. 77 (2015) 48–57.

[65] C.W. Hirt, B.D. Nichols, Volume of fluid (VOF) method for the dynamics of free boundaries, J. Comput. Phys. 39 (1981) 201–225.

[66] H.H. Weller, A New Approach to VOF-based Interface Capturing Methods for Incompressible and Compressible Flow, OpenCFD Ltd, 2008. Report TR/HGW/04.

[67] F.-Y. Zhang, D. Spernjak, A.K. Prasad, S.G. Advani, In situ characterization of the catalyst layer in a polymer electrolyte membrane fuel cell, J. Electrochem. Soc. 154 (2007) B1152–B1157.

[68] S. Ma, C.-H. Solterbeck, M. Odgaard, E. Skou, Microscopy studies on pronton exchange membrane fuel cell electrodes with different ionomer contents, Appl. Phys. A 96 (2009) 581–589.

[69] The OpenFOAM Foundation, 2017. http://www.openfoam.org/ (accessed 22 February 2017).

[70] E.E. Petersen, Diffusion in a pore of varying cross section, AIChE J. 4 (1958) 343–345.

[71] S. Litster, W. Epting, E. Wargo, S. Kalidindi, E. Kumbur, Morphological analyses of polymer electrolyte fuel cell electrodes with nano-scale computed tomography imaging, Fuel Cells 13 (2013) 935–945.

[72] Avizo User Guide 2013, 2017. https://www.fei.com/ (accessed 22 February 2017).